Int. J. Heat Mass Transfer. Vol. 31, No. 6, pp. 1221–1235, 1988
Printed in Great Britain

0017-9310/88 $3.00 + 0.00

Scaling theory of melting with natural convection in an enclosure

PETER JANY and ADRIAN BEJAN
Department of Mechanical Engineering and Materials Science, Duke University, Durham, NC 27706, U.S.A.

(*Received* 18 *August* 1987 *and in final form* 5 *November* 1987)

Abstract—This study identifies the most basic scales and regimes of the phenomenon of melting with natural convection in an enclosure heated from the side. In the first part of the study the method of scale analysis is used to show that the phenomenon consists of a sequence of four regimes: (a) the pure conduction regime, (b) the mixed regime in which the upper portion of the liquid gap is ruled by convection and the lower portion by conduction, (c) the convection regime and, finally, (d) the last or 'shrinking solid' regime. For the first three regimes the scaling theory predicts a Nusselt number vs time curve that has features similar to a van der Waals isotherm, in particular, a clear Nu minimum of order $Ra^{1/4}$ at a time $Ste\,Fo$ of order $Ra^{-1/2}$, where Ste is the liquid superheat Stefan number and Fo the Fourier number based on H. The corresponding average melting front position has an inflexion point at a time of order $Ra^{-1/2}$. The theory shows further that during the fourth regime the solid disappears during a $Ste\,Fo$ time interval of order $Ra^{-1/4}$. The second part of the study consists of numerical experiments the purpose of which is to verify the correctness of the theory constructed in the first part. The numerical simulations are based on the quasi-stationary front approximation and the quasi-steady natural convection assumption. The parametric domain covered by these simulations is $0 \leqslant Ra \leqslant 10^8$, $0 < Ste\,Fo < 0.2$, $Pr = 50$ and $H/L = 1$, where L is the horizontal dimension of the enclosure and Ra the Rayleigh number based on H. Closed form correlations for both Nu and the melting front location time functions are developed by combining the theoretical and numerical conclusions of the study.

OBJECTIVE

THE PROGRESS on natural convection dominated phase-change heat transfer was reviewed most recently by Viskanta [1, 2]. To the newcomer these reviews unveil a field that is already voluminous, established and blessed with a long string of important engineering applications. Yet, one general conclusion that emerges from these reviews is that natural convection and phase-change phenomena are quite complicated, to the point that "no unified theoretical treatment ... is within our grasp" (p. 846 of Viskanta [2]). The complications stem primarily from the strong coupling between the natural circulation of the liquid phase and the melting rate of the solid. It is this coupling that determines the instantaneous shape of the liquid–solid interface, which becomes one of the key unknowns in each problem.

In natural convection melting of a solid heated from the side the liquid–solid interface changes its shape and position continually (Fig. 1). The variation of the geometry of the system is chiefly responsible for the peculiar character of the heat transfer measurements that have been reported. The common features of these measurements are revealed also by the present numerical Nusselt number calculations, which are illustrated in Figs. 5 and 8. In time, the overall Nusselt number describes a wavy curve with features similar to those of a van der Waals isotherm. These features have proven to be very puzzling, because so far it has been impossible to correlate the wavy Nusselt number curves in terms of the dimensionless parameters suggested by routine dimensional analysis.

The most comprehensive and focused effort of constructing a unifying correlation for heat transfer and melting rates in cavities heated from the side was reported by Webb and Viskanta [3]. These authors tried several correlation methods, using either the height of the enclosure (H) or the average thickness of the liquid zone (s_{av}) as the characteristic length scale. They showed that the classical methods fail to correlate adequately the heat transfer results over the entire time domain. Attributing this failure to the probable use of incorrect length scales, Webb and Viskanta [3] concluded with the following:

> "Caution is therefore advised when using correlations in the literature for design purposes or as quantitative comparisons with independent investigators. The proper characteristic length in melting/solidification needs more research attention."

These final words sum up the motivation for undertaking the present study. Its objective is (1) to identify the correct scales of the phenomenon and (2) to use these scales in order to construct a heat transfer correlation that covers successfully the entire time domain.

SCALE ANALYSIS

The key to the correct correlation of seemingly complicated trends such as those of convection melting is

NOMENCLATURE

c_1, c_2 empirical constants, equations (37)
c_1', c_2' empirical constants, equations (64) and (65)
C constant for Neumann's solution, equation (8)
C_1 empirical constant, equation (53)
Fo Fourier number, equation (4)
g gravitational acceleration
h height of solid region
h_{sf} latent heat of fusion
H height of enclosure
k liquid thermal conductivity
l horizontal dimension of solid region
L horizontal dimension of enclosure
m empirical constant, equation (40)
n empirical constant, equation (37)
Nu Nusselt number, equation (5)
Nu_{min} minimum Nusselt number, equation (23)
Pr Prandtl number
Q total heat transfer rate
Q_c convective heat transfer rate
Ra Rayleigh number based on H, $g\beta(T_w - T_s)H^3/(\alpha\nu)$
Ra_h Rayleigh number based on h, $g\beta(T_w - T_s)h^3/(\alpha\nu)$
Ra_l Rayleigh number based on l, $g\beta(T_w - T_s)l^3/(\alpha\nu)$
s melting front position
s_{av} average melting front position, equation (26)
s_{top} melting front position measured along the top wall
S dimensionless melting front position, s/H
S_{av} dimensionless average melting front position, s_{av}/H
Ste liquid superheat Stefan number, equation (4)
t time
T temperature
T_s interface (melting) temperature
T_w warm wall temperature
u horizontal velocity
v vertical velocity
x horizontal coordinate
y vertical coordinate
z height of the convection dominated liquid region.

Greek symbols
α thermal diffusivity
β coefficient of volumetric thermal expansion
δ_z thermal boundary layer thickness in convection zone of height z
θ dimensionless time, equation (3)
θ_0 time of end of conduction, equation (33)
θ_1 time marking the end of the mixed regime, equation (22)
θ_2 time when the top wall is bathed fully by liquid, equation (29)
θ_3 time when the solid disappears
θ_{min} time when Nu reaches its minimum value, equation (24)
ν kinematic viscosity
ξ transformed horizontal coordinate, equation (41)
ρ density
ψ streamfunction
Ψ dimensionless streamfunction, ψ/ν.

the identification of the proper scales of the phenomenon. Consider the time-dependent melting of an energy storage phase-change material in a vertical rectangular enclosure heated from the side (Fig. 1). Initially, the $H \times L$ enclosure is filled entirely by the solid phase, the initial temperature T_s of which is uniform. For simplicity we assume also that T_s is the same as the fusion temperature of the material, in other words, we assume that the degree of solid subcooling is zero. Beginning with the time $t = 0$, the left wall of the enclosure is heated and maintained at a constant temperature level T_w. This heating effect causes both melting at the liquid–solid interface and natural convection in the region carved out for itself by the liquid phase.

The other assumptions on which this study is based are: (i) the liquid flow is laminar and two-dimensional, (ii) the density difference between the liquid and solid phases is negligible, (iii) the liquid has a Prandtl number greater than one, and (iv) the properties are all constant, with the exception of the linear density–temperature relation assumed in the buoyancy term of the momentum equation (the Boussinesq approximation).

The conduction limit

It is well understood that immediately after $t = 0$ the melting process is ruled by pure conduction [1–3]. The horizontal heat flux across the incipient vertical liquid film is balanced entirely by the enthalpy absorbed at the liquid–solid interface (see the Nomenclature)

$$k\frac{T_w - T_s}{s} \sim \rho h_{sf}\frac{ds}{dt}. \quad (1)$$

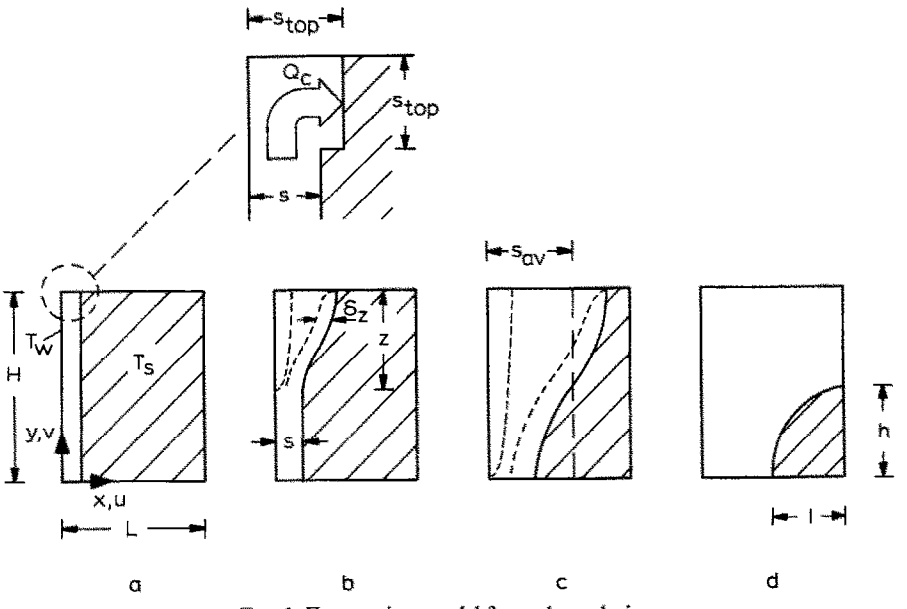

FIG. 1. Four-regime model for scale analysis.

Equation (1) shows that from the beginning the liquid layer thickness is a function of time

$$s \sim \left[\frac{k(T_w - T_s)t}{\rho h_{sf}}\right]^{1/2} \sim H\theta^{1/2} \tag{2}$$

where θ is the dimensionless time

$$\theta = \frac{c(T_w - T_s)}{h_{sf}}\frac{\alpha t}{H^2}. \tag{3}$$

According to the usual terminology of phase-change heat transfer, the dimensionless time θ is the same as the product of the Stefan and Fourier numbers, $\theta = Ste\,Fo$, where Ste measures the degree of liquid superheat and Fo the time of thermal diffusion across the distance H

$$Ste = \frac{c(T_w - T_s)}{h_{sf}}, \quad Fo = \frac{\alpha t}{H^2}. \tag{4}$$

The Nusselt number that corresponds to this pure conduction limit is

$$Nu = \frac{Q}{k(T_w - T_s)} \sim \frac{H}{s} \sim \theta^{-1/2} \tag{5}$$

where Q is the total heat transfer rate through the left wall of the enclosure, per unit length in the direction normal to the plane of Fig. 1(a).

The preceding results do not add anything to what we know already from Neumann's exact solution [4]

$$\frac{s}{H} = 2C\,Fo^{1/2} \tag{6}$$

$$Nu = [\mathrm{erf}(C)]^{-1}\pi^{-1/2}\,Fo^{-1/2} \tag{7}$$

where C is an implicit function of the Stefan number

$$Ste = \pi^{1/2}C\frac{\mathrm{erf}(C)}{\exp(-C^2)}. \tag{8}$$

The purpose of the scale analysis represented by equations (1)–(5) is to show that its predictions agree within a factor of order one with the results of the corresponding exact solution (for more on this see pp. 17–21 of ref. [5]). Note that in the $Ste \to 0$ limit the exact solution, equations (6)–(8), reduces to

$$\frac{H}{s} = Nu = (2\theta)^{-1/2} \tag{9}$$

that is, to results that agree within a factor of order one with equation (2).

Before abandoning the pure conduction limit, it is worth noting that an infinitesimally small convection heat transfer effect is present even in the limit $\theta \to 0$. Consider the slender vertical cavity of height H and thickness s, the liquid content of which is exposed to the horizontal temperature difference $(T_w - T_s)$. Assuming that the coefficient of volumetric thermal expansion of the liquid (β) is positive, the liquid will circulate clockwise in a very slender 'cell' of size $H \times s$. The vertical velocity scale of this very slender counterflow, v, is determined by the balance between the vertical buoyancy effect $g\beta(T_w - T_s)$ and the vertical friction effect in a gap of thickness s (namely, $\nu v/s^2$). The resulting velocity scale is

$$v \sim \frac{g\beta(T_w - T_s)}{\nu}s^2 \tag{10}$$

in which $s(t)$ is given by equation (2).

The convective heat transfer rate carried upward by this counterflow is

$$Q_c \sim (\rho s v)c(T_w - T_s) \tag{11}$$

in which (ρsv) represents the vertical mass flow rate of one branch. The weak convective heat current Q_c originates from the bottom end of the hot wall, flows vertically through the s-wide gap and, ultimately, is absorbed by the top end of the cold wall (in our case, by the top end of the liquid–solid interface). The total heat transfer rate in the horizontal direction, that is, through the H-tall liquid gap, is the sum of the conduction and convection contributions

$$Q \sim kH\frac{T_w - T_s}{s} + Q_c. \tag{12}$$

Noting the Nusselt number definition (5), this Q estimate translates into

$$Nu \sim \theta^{-1/2} + Ra\,\theta^{3/2} \quad (\theta \to 0). \tag{13}$$

The convection contribution $(Ra\,\theta^{3/2})$ participates in the sum (13) with a numerical coefficient of order one, which is not shown. The important conclusion is that relative to the dominant effect of pure conduction $(\theta^{-1/2})$ the convective contribution increases with time.

The mixed conduction plus convection regime

The deformation of the rectangular shape of the liquid zone is from the beginning the result of the convective heat transfer contribution Q_c. In order to see this consider again the $\theta \to 0$ limit, which geometrically translates into the infinitely slender enclosure limit, $H/s \to \infty$. In this geometric limit the flow field consists of a slender counterflow of height H terminated by two end regions the height of which is of the same order as the transversal dimension of the counterflow [6, 7]. Let s_{top} be the length scale of the enlarged top end region (Fig. 1(a)). The top portion of the liquid–solid interface melts faster on account of Q_c, which must 'sink' into the top end region. Writing that the melting rate of the s_{top}-tall portion of the interface is ruled by Q_c plus the conduction heat transfer collected over the height s_{top}

$$ks_{top}\frac{T_w - T_s}{s_{top}} + Q_c \sim s_{top}\rho h_{sf}\frac{ds_{top}}{dt} \tag{14}$$

using equations (10) and (11) we obtain

$$s_{top} \sim H(\theta + Ra\,\theta^{5/2})^{1/2} \quad (\theta \to 0) \tag{15}$$

in other words

$$\frac{s_{top}}{s} \sim (1 + Ra\,\theta^{3/2})^{1/2}$$

$$\sim 1 + O(Ra\,\theta^{3/2}) \quad (\theta \to 0). \tag{16}$$

This result shows that from the beginning the top portion of the liquid–solid interface recedes faster than the remainder of the interface. It is known that if the horizontal dimension of a rectangular enclosure (with fixed Ra) increases monotonically, the conduction heat transfer regime gives way eventually to the convection regime, in which both sides of the enclosure are lined by distinct thermal boundary layers (see, e.g. p. 166 of ref. [5]). Equation (16) shows that the convection regime will set in starting from the top of the liquid space.

Let the unknown vertical dimension z be the height of the upper region that has become wide enough to be ruled by convection. The heat transfer across the remainder of the liquid space (height $= H - z$, Fig. 1(b)) continues to be ruled by conduction. Now, convection in the upper zone means that the thermal boundary layer thickness in this zone, δ_z, is smaller than the horizontal dimension of the carved-out upper zone. The convective zone expires at its lower extremity, where δ_z is of the same order as the gap thickness of the lower (conduction) zone

$$\delta_z \sim s, \text{ at the convection–conduction transition level.} \tag{17}$$

In equation (17) we have the means for estimating the height of the convection-dominated region, z. Since the liquid has a Prandtl number greater than one, we have

$$\delta_z \sim z\,Ra_z^{-1/4} \tag{18}$$

where Ra_z is the Rayleigh number based on z, namely $Ra_z = g\beta z^3(T_w - T_s)/(\alpha\nu)$ or $Ra_z = (z/H)^3\,Ra$. Combining equations (17) and (18) with equation (2) for the conduction gap s, yields

$$z \sim H\,Ra\,\theta^2. \tag{19}$$

In conclusion, the convection zone expands downward as the time increases. The expansion is faster at higher Rayleigh numbers. Note further that this expansion phenomenon meshes very well with the growth of the square-end top region of the conduction limit, equation (16) and Fig. 1(a). Also worth noting is the relation $z/s \sim Ra\,\theta^{3/2}$.

Regarding the total heat transfer rate through the heated wall, Q, we note that the heat transfer mechanism is convection over the height z and conduction over $(H - z)$. The total heat transfer rate is therefore the sum

$$Q \sim kz\frac{T_w - T_s}{\delta_z} + k(H - z)\frac{T_w - T_s}{s} \tag{20}$$

which, in view of equations (2), (5), (18) and (19) translates into

$$Nu \sim \theta^{-1/2} + Ra\,\theta^{3/2}. \tag{21}$$

As expected, the Nusselt number is made up of two contributions, one due to conduction and the other to convection. One rewarding feature of equation (21) is that it meshes perfectly with the scaling law that holds in the $\theta \to 0$ limit, equation (13). This time, however, the convection contribution $(Ra\,\theta^{3/2})$ is not necessarily negligible when compared with the conduction contribution $(\theta^{-1/2})$.

In conclusion, the heat transfer scaling law (21) holds starting with $\theta = 0$ until the assumed convection zone (height z) extends all the way to the bottom of

the liquid space, that is, until $z \sim H$. If we label θ_1 the time scale that corresponds to $z \sim H$, equation (19) suggests that the mixed conduction plus convection regime ends at a time of order

$$\theta_1 \sim Ra^{-1/2}. \tag{22}$$

In the time interval $(0, \theta_1)$ in which it is valid, the Nusselt number scaling law (21) distinguishes itself through *the analytical prediction of an Nu minimum* of order

$$Nu_{\min} \sim Ra^{1/4} \tag{23}$$

which occurs at a time of order

$$\theta_{\min} \sim Ra^{-1/2} \tag{24}$$

i.e. at the end of the mixed heat transfer regime, $\theta_{\min} \sim \theta_1$. These scales follow from applying $\partial Nu/\partial\theta = 0$ to equation (21).

The convection regime

At times greater than θ_1 the convection-dominated zone fills the entire liquid space of height H. Distinct boundary layers line both the (T_w) wall and the (T_s) phase-change interface (Fig. 1(c)). Since $Pr > 1$, the overall Nusselt number scale is

$$Nu \sim Ra^{1/4}. \tag{25}$$

This scaling law holds even though the phase-change interface is deformed and continues to deviate from the vertical plane shape. It is known that the boundary-layer convection scaling law (25) works very well also for curved surfaces, provided Ra is based on a length scale of the same order as the vertical dimension of the surface [8].

The heat transfer rate (25) is related to the speed with which the melting front advances to the right, $\mathrm{d}s/\mathrm{d}t$. Since in the convection regime the melting front is always deformed, $s(y, t)$, it is more appropriate to argue in terms of the height-averaged melting front location

$$s_{av}(t) = \frac{1}{H}\int_0^H s(y, t)\,\mathrm{d}y. \tag{26}$$

Writing that the total heat transfer rate Q is used for the purpose of displacing the melting front to the right

$$Q \sim \rho h_{sf} H \frac{\mathrm{d}s_{av}}{\mathrm{d}t} \tag{27}$$

and noting that equation (25) means $Q \sim Ra^{1/4}k \times (T_w - T_s)$, we arrive at the scaling law for the convection-driven interface.

$$s_{av} \sim H Ra^{1/4}\theta. \tag{28}$$

In a system of finite horizontal extent, L, the scenario concluded with equations (25) and (28) holds until the liquid–solid interface reaches the right wall, $s_{av} \sim L$. Let θ_2 represent the time scale associated with this event. Equation (28) yields immediately

$$\theta_2 \sim \frac{L}{H} Ra^{-1/4}. \tag{29}$$

The convection regime exists only if $\theta_2 > \theta_1$, that is, if

$$Ra^{1/4} > \frac{H}{L}. \tag{30}$$

When this criterion is not satisfied (i.e. when $\theta_2 < \theta_1$) the mixed conduction plus convection regime of Fig. 1(b) ends at a time of order θ_2, that is, before the $Nu(\theta)$ curve has had time to reveal its minimum. That criterion (30) and the Nu minimum are threatened as Ra decreases is clearly illustrated by the numerical $Nu(\theta)$ curves plotted in Figs. 5 and 8. Worth noting also is that equations (29) and (30) and, for that matter, all the other convection scales described in this paper are valid provided the Rayleigh number is small enough to prevent the transition to turbulent natural convection boundary layer flow. Criteria for predicting the transition Rayleigh number are reviewed in ref. [9].

What happens after the melting front reaches the right wall, $\theta > \theta_2$, constitutes a distinct heat transfer regime the main features of which are sketched in Fig. 1(d). For a better balance between scaling theory and numerical experiment, we postponed the discussion of this last regime until we had a chance to test numerically the validity of the predictions made up till now.

NUMERICAL VERIFICATION OF THE SCALING RESULTS

In parallel with the theoretical consideration of the phenomenon of natural convection melting in an enclosed space, we conducted a series of numerical simulations of the Ra range 0–10^8 in a square box and at a Stefan number of order 0.1. The numerical formulation of the problem is standard, therefore, we make no claim concerning its originality. In the interest of succinctness we say only that the numerical procedure was based additionally on the so-called quasi-steady natural convection approximation [10]. The numerical results developed in this way are valid in the limit of negligible liquid thermal inertia, namely, $Ste \to 0$. The details of the numerical formulation and procedure are stored in ref. [11].

One test of the numerical solutions consisted of comparing the calculated average melting front location

$$S_{av}(\theta) = \int_0^1 S(\theta, Y)\,\mathrm{d}Y \tag{31}$$

with experimental and numerical results reported by other investigators. For this reason the Prandtl number was fixed at $Pr = 50$, which is representative of the Pr range of n-octadecane [12]. The actual value of Pr is not crucial in the testing of the preceding scaling theory, provided $Pr > O(1)$.

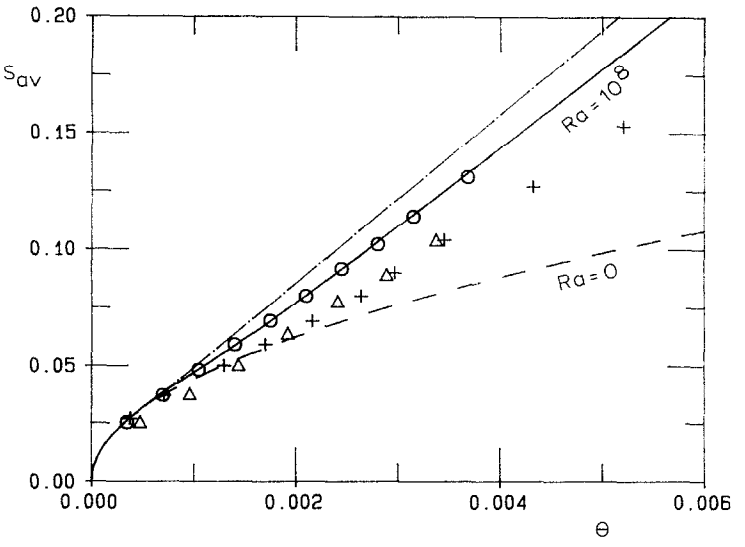

FIG. 2. Comparison between numerical results and experimental measurements: Δ, $Ste = 0.09$, $Ra = 10^8$ [10]; ○, $Ste = 0.09$, $Ra = 10^8$ [13]; +, $Ste = 0.1$, $Ra = (8.9)10^7$ [15]; —·—, $Ste = 0.2$, $Ra = 10^8$ [14].

Figure 2 shows the results of this comparison in the case of a high Rayleigh number ($Ra = 10^8$) and in the relatively short-time interval $0 < \theta < 0.006$ in which the heat transfer mechanism had had enough time to pass through the conduction, mixed and convection regimes (Figs. 1(a)–(c)). The present results fall right on top of the numerical results of Kassinos and Prusa [13]. Both sets of results fall slightly below Gadgil and Gobin's [14] calculations, which is understandable in view of the fact that in Gadgil and Gobin's study the top surface of the liquid pool was modeled as free (zero shear), in contrast to the no-slip condition used here. The same figure shows that the experimental results published by Ho and Viskanta [10] and Bareiss and Beer [15] fall below the present calculations, some of them falling below even the pure conduction solution $Ra = 0$. Not shown in this figure are Ho and Viskanta's numerical results for the same case, which also fall below the present results (the solid line) as well as those of Kassinos and Prusa [13].

In Fig. 3 the present results are compared with those of Okada [16] at a lower Rayleigh number and over a much longer time interval, $0 < \theta < 0.045$. The interesting fact here is that the slopes of the numerical and experimental curves for $Ra = (5.34)10^6$ are nearly the same. It is possible that the true starting point of Okada's curve (the crosses) is somewhere between our $\theta = 0$ and 0.005, because any enclosure-type apparatus has a 'time constant' that separates the moment when the heating effect is applied to the wall from the moment when the contents of the enclosure begin to experience this heating effect. Worth noting is that if Okada's curve is shifted enough to the left so that it becomes, as it should be, tangent to the pure conduction solution $Ra = 0$, then the numerical and experimental curves agree very well.

The numerical results that are most relevant from a heat transfer engineering standpoint are the evolution of the average melting front location (Fig. 4), and the Nusselt number averaged over the heated vertical wall (Fig. 5). In all the runs the aspect ratio of the enclosure was held fixed at $H/L = 1$. The description of the numerical solutions for the flow pattern in the liquid zone is omitted for the sake of conciseness: these patterns differ little from what was revealed by experiments [10, 12–16] and by Okada's extensive study [17].

The family of five $S_{av}(\theta)$ curves of Fig. 4 shows the manner in which the liquid zone expands into the solid as the time increases. Especially at high Rayleigh numbers, each curve is roughly a straight line with a slight undulation: this and the orientation (slope) of the curve are anticipated by the scale analysis of the first three heat transfer regimes. One important point along each $S_{av}(\theta)$ curve is the point marked with a filled circle: this point corresponds to the time when the uppermost section of the liquid–solid interface first touches the vertical adiabatic boundary of the system. For reasons that are explained in the next paragraph and Fig. 5, we label this special time θ_{knee} and recognize that according to equation (29) θ_{knee} must be of the same order of magnitude as θ_2. The second row of points in Fig. 6 shows that indeed the ratio θ_{knee}/θ_2 is of the order of one.

Figure 5 shows how the Rayleigh number affects the shape and position of the Nusselt number vs time curve. Although defined in the beginning of equation (5), the numerical solution version of the definition of Nu is

$$Nu = -\int_0^1 \left(\frac{\partial T_*}{\partial X}\right)_{X=0} \mathrm{d}Y. \tag{32}$$

Each $Nu(\theta)$ curve has the features anticipated in the scale analysis section, first, the pure conduction decay of order $\theta^{-1/2}$, followed by the mixed regime with its

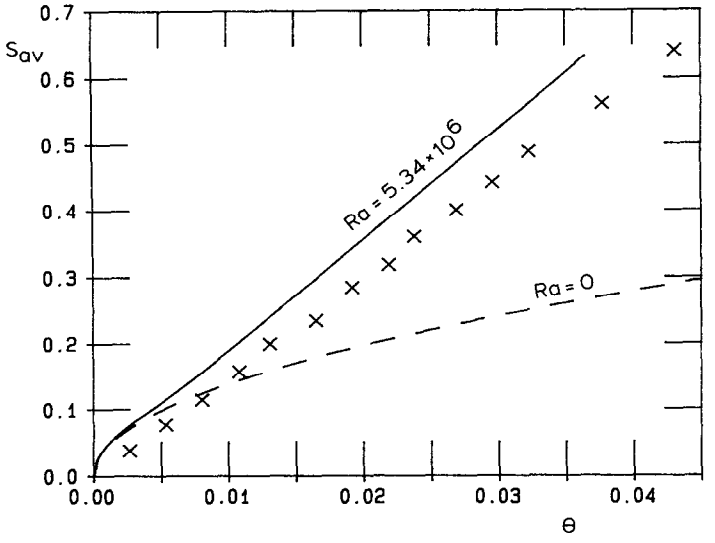

FIG. 3. Comparison between numerical results and experimental measurements: ×, $Ste = 0.0921$, $Ra = (5.34)10^6$ [16].

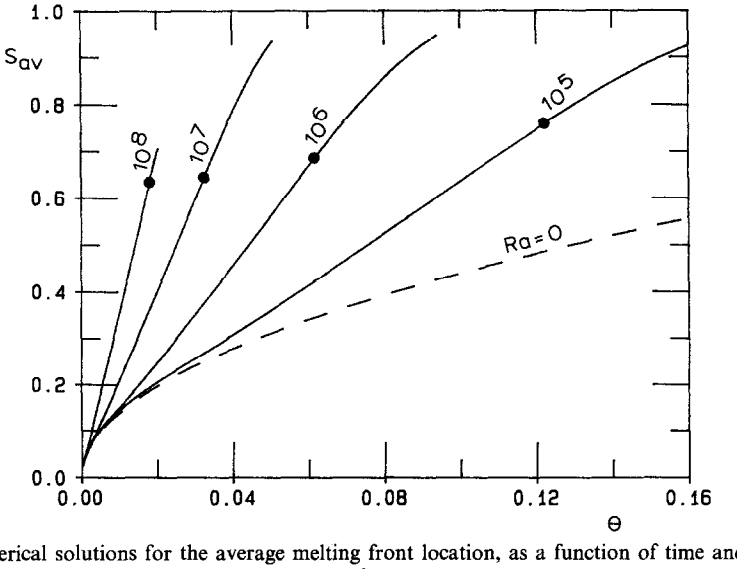

FIG. 4. Numerical solutions for the average melting front location, as a function of time and Rayleigh number.

Nu minimum and, finally, the pure convection *Nu* plateau of order $Ra^{1/4}$. The Nusselt number curve changes slope as it passes through the 'knee' point where the melting front first touches the right-hand side adiabatic boundary. The time associated with this event is θ_{knee}. At times greater than θ_{knee} the Nusselt number decreases relatively fast and almost linearly in time, as described in the section on the fourth (shrinking solid) regime.

Figure 6 tests the correctness of some of the scaling laws developed in the theoretical part of this study. The first row of points shows that the time of the Nusselt number minimum, θ_{min}, is indeed of the order of θ_1, as anticipated in equations (22) and (24). It is interesting to note that the θ_{min} scale agrees very well with what Bénard *et al.* [18] called the time of 'end of conduction'. For the end-of-conduction time scale Bénard *et al.* reported an empirical correlation, which in the present notation reads

$$\theta_0 = 4.59 Ra^{-1/2}. \tag{33}$$

They estimated the θ_0 values for this correlation by intersecting the horizontal pure-convection plateau of each Nusselt number curve (Fig. 5) with the pure-conduction asymptote (9) shared by all these curves. Since, according to Fig. 6, our θ_{min} scale is approximately $9Ra^{-1/2}$, we conclude that Bénard *et al.*'s end-of-conduction time scale is equal to half of the θ_{min} scale.

Continuing with the reading of Fig. 6, we see that the third row of points uses the knee-point Nusselt number (Nu_{knee}) to show that in the pure convection

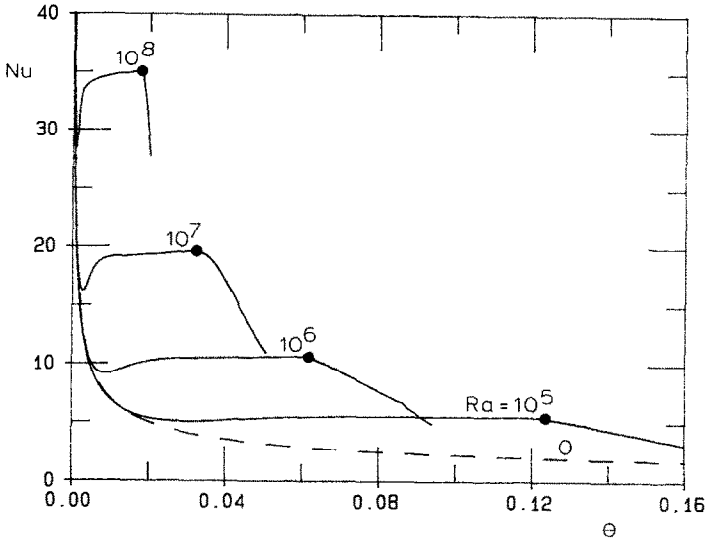

FIG. 5. Numerical solutions for the average Nusselt number at the heated wall, as a function of time and Rayleigh number.

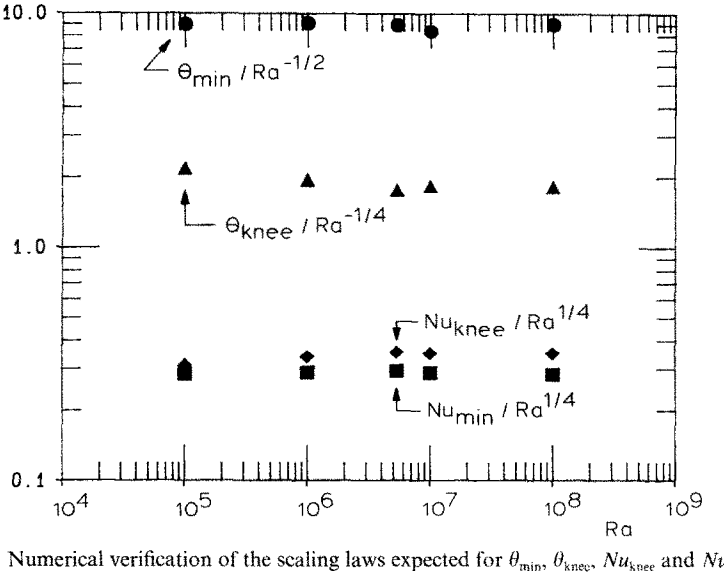

FIG. 6. Numerical verification of the scaling laws expected for θ_{min}, θ_{knee}, Nu_{knee} and Nu_{min}.

limit the Nusselt number scales as $Ra^{1/4}$, equation (25). Furthermore, the last row in Fig. 6 shows that Nu_{min} scales as $Ra^{1/4}$, as anticipated in equation (23).

An overall test of the correctness of the fluid mechanics scaling results has been constructed in Fig. 7. This figure shows the calculated streamfunction maximum, Ψ_{max}, as a dimensionless measure of the flow rate of the liquid circulation. The figure was constructed knowing first that in the pure conduction limit $\psi \sim vs$, where s and v are given by equations (2) and (10). In the dimensionless Ψ notation shown in the Nomenclature this means

$$\Psi \sim \frac{Ra}{Pr}\theta^{3/2} \quad \text{(conduction)}. \tag{34}$$

On the other hand, in the pure convection limit $\psi \sim v\delta$, where $v \sim (\alpha/H)Ra^{1/2}$ and $\delta \sim Pr^{1/2}H\,Ra^{1/4}$ (p. 120 of ref. [5], the case $Pr > 1$), therefore

$$\Psi \sim Pr^{-1/2}\,Ra^{1/4} \quad \text{(convection)}. \tag{35}$$

Intersecting equations (34) and (35) we learn that the 'knee' of each Ψ vs θ curve is located at $\theta \sim Ra^{-1/2}$. Recalling that Pr has been held fixed, these equations imply that all the $\Psi(\theta, Ra)$ curves should collapse onto a single curve if plotted as $\Psi/Ra^{1/4}$ vs $\theta\,Ra^{1/2}$. Figure 7 shows that this is indeed the case and that the knee of this correlating curve is located in the domain where the abscissa parameter $\theta\,Ra^{1/2}$ is of the order of one.

HEAT TRANSFER CORRELATION

The Nusselt number and time scales tested in Figs. 4–6 provide the necessary backbone on which to con-

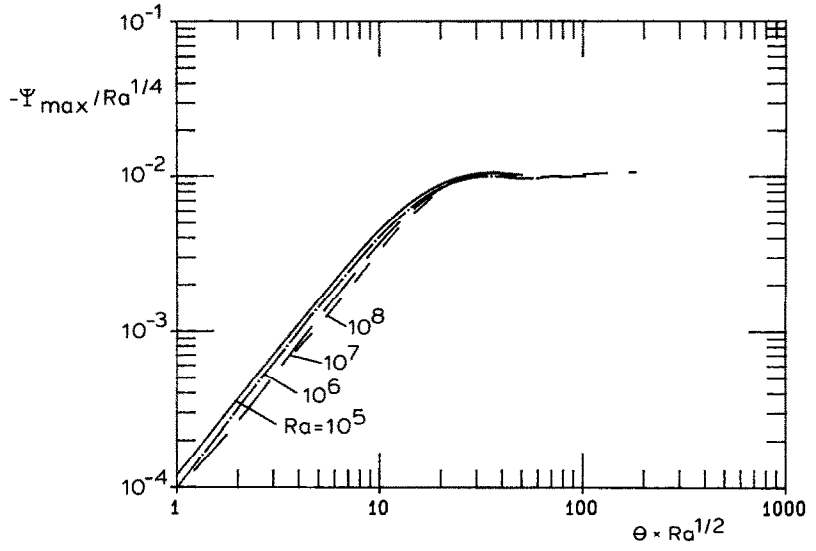

FIG. 7. Scaling correct correlation of the evolution of the streamfunction maximum.

struct a heat transfer correlation that spans the conduction, mixed and convection regimes. In the conduction regime ($\theta \ll \theta_1$) the Nusselt number must approach the asymptote $(2\theta)^{-1/2}$, equation (9). In the mixed conduction plus convection regime ($\theta \sim \theta_1$) the $Nu(\theta)$ passes through a minimum of order $Ra^{1/4}$. In the pure convection regime ($\theta_1 < \theta < \theta_2$) the Nusselt number is time independent and of order $Ra^{1/4}$. These three types of Nu vs θ behavior are explicitly evident in the single correlation

$$Nu = (2\theta)^{-1/2} + [c_1 Ra^{1/4} - (2\theta)^{-1/2}][1 + (c_2 Ra^{3/4}\theta^{3/2})^n]^{1/n}. \quad (36)$$

The second pair of square brackets on the right-hand side of this correlation contains a canonical expression of the type recommended by Churchill [19]. That equation (36) reproduces the analytical asymptotes of the three heat transfer regimes (equations (9), (21) and (25)) can be seen while keeping in mind that n is an empirical exponent the value of which must be negative. For example, at large θ's the second pair of square brackets approaches the value 1, therefore equation (36) approaches the pure convection scaling law $Nu = c_1 Ra^{1/4}$. This limit allows us to evaluate c_1 as the ratio $Nu/Ra^{1/4}$ associated with the knee points of the curves of Fig. 5, that is, with the most distant states of pure convection. The average $Nu_{knee}/Ra^{1/4}$ value displayed already in Fig. 6 is 0.35. The remaining constants, c_2 and n, were evaluated empirically by fitting equation (36) to the Nusselt number minima of the $Nu(\theta)$ curves. In summary, the three constants that allow the three-regime correlation (36) to cover the time domain $0 < \theta < \theta_2$ are

$$c_1 = 0.35, \quad c_2 = 0.0175, \quad n = -2. \quad (37)$$

The smooth lines plotted in Fig. 8 show that the correlation, equations (36) and (37), summarizes very well the Nusselt number numerical results developed for the entire Ra range 0–10^8. One remarkable feature of this correlation is that in the $\theta < \theta_2$ range the Nusselt number does not depend on the geometric aspect ratio H/L. On the one hand, this feature should be expected since at times θ smaller than θ_2 the natural circulation in the liquid zone is unaware of L as a horizontal length scale. On the other hand, it is well known that in pure natural convection in rectangular enclosures (without melting) the aspect ratio of the fluid space plays an additional albeit minor effect on the convection scaling law assumed in equation (25) [20]. With respect to the instantaneous geometry of the liquid zone in the convection dominated regime of the present problem (height H, horizontal thickness s_{av}) the more complete heat transfer scaling law to consider in place of equation (25) is (ref. [20]; also p. 173 of ref. [5])

$$\frac{Nu}{Ra^{1/4}} = f\left[\left(\frac{H}{s_{av}}\right)^{4/7} Ra^{1/7}\right] \quad (38)$$

where function f has a dimensionless value of the order of 0.3. Worth noting is that f decreases slightly as the time increases and the average aspect ratio H/s_{av} decreases. This effect has been neglected in the theory that led to correlation (36), and this is why that correlation is independent of an 'aspect ratio' until $\theta \sim \theta_2$.

CORRELATION FOR THE AVERAGE MELTING FRONT LOCATION

The $S_{av}(\theta)$ curves of Fig. 4 could be correlated similarly, by recognizing the scaling–correct analytical form of the $S_{av}(\theta)$ function in each of the three heat transfer regimes that precede the knee point, $\theta \sim \theta_2$. It turns out that the same job is done even better by a

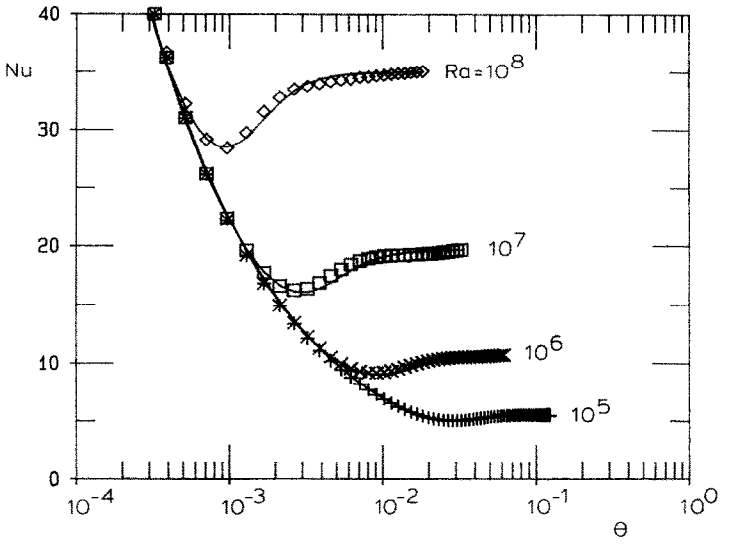

FIG. 8. The match between the heat transfer correlation, equations (36) and (37), and the numerical *Nu* results of Fig. 5.

simpler correlation based on only the pure conduction and pure convection asymptotes

$$S_{av} = \{[(2\theta)^{1/2}]^m + [c_1 Ra^{1/4}\theta]^m\}^{1/m}. \quad (39)$$

We see here again the canonical form recommended by Churchill [19] and, quite clearly, the asymptotic forms of the $S_{av}(\theta)$ function. The empirical constants that allow equation (39) to summarize best the $\theta < \theta_2$ information of Fig. 4 are

$$c_1 = 0.35 \quad \text{and} \quad m = 5 \quad (40)$$

where c_1 is the same as in the preceding *Nu* correlation. Figure 9 shows that the average melting front location correlation (39) fits the numerical results very well.

THE FOURTH (SHRINKING SOLID) REGIME

We turn our attention now to the fourth regime sketched in Fig. 1(d), in which the remaining solid shrinks as its uppermost point ($y = h$) descends along the right-hand wall. The liquid circulation is always in the convection regime, however, the heat transfer and melting rates depend on the size of the remanent solid.

In order to determine the scales of this last regime it is necessary to make an assumption concerning the shape of the solid region. Let us assume first that early enough in this regime the cross-section of the solid is roughly a triangle the hypotenuse of which pivots

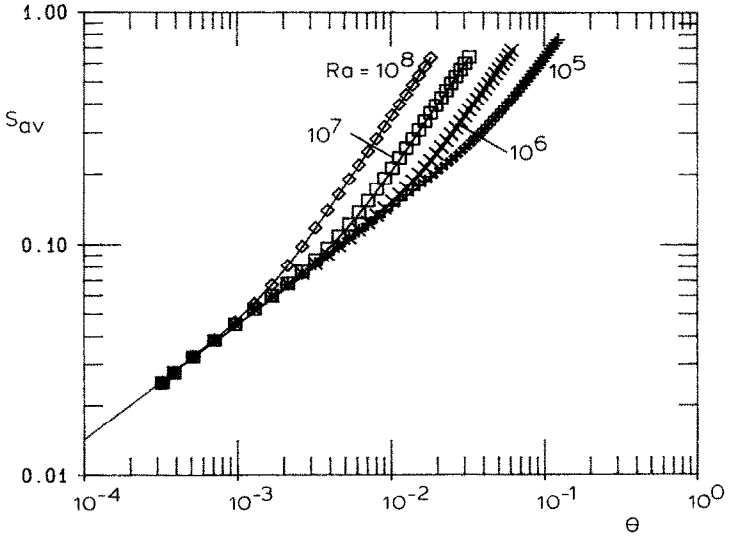

FIG. 9. The match between the S_{av} correlation, equations (39) and (40), and the numerical results of Fig. 4.

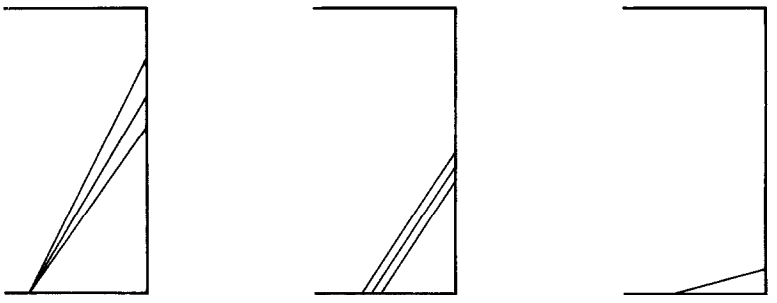

FIG. 10. Three assumptions concerning the shape of the solid region during the fourth regime (Fig. 1(d)).

about the bottom end of the liquid–solid interface (Fig. 10(a)). In other words, the solid cross-section scales as the product lh, in which l is fixed. The heat transfer rate across the liquid space is impeded by two thermal resistances in series, the thermal boundary layer resistance along the heated wall (of order $Ra^{-1/4}$) and the corresponding resistance along the liquid–solid interface, which is of order $Ra_h^{-1/4}$; since $Ra_h^{-1/4} > Ra^{-1/4}$, it is the interface resistance that controls the heat transfer rate that melts the solid. The energy balance at the moving interface states then

$$k(T_w - T_s)\, Ra_h^{1/4} \sim \rho h_{sf}\left[-\frac{d(lh)}{dt}\right] \tag{41}$$

where the minus sign in the square brackets is necessary in order to make the right-hand side of equation (41) positive (note that h decreases with time). Rewritten in dimensionless notation equation (41) becomes

$$\frac{H}{l} Ra^{1/4} \sim -\left(\frac{h}{H}\right)^{-3/4} \frac{d}{d\theta}\left(\frac{h}{H}\right) \tag{42}$$

which, integrated after the knee point time $\theta \sim \theta_2$ (when $h/H \sim 1$), yields approximately

$$\left(\frac{h}{H}\right)^{1/4} \sim 1 - \frac{H}{l} Ra^{1/4}(\theta - \theta_2). \tag{43}$$

This result shows that the height of the solid region decreases as the time increases beyond θ_2. The solid promises to disappear entirely at a time θ_3 when $(h/H) \ll 1$, which, according to equation (43), means

$$\theta_3 - \theta_2 \sim \frac{l}{H} Ra^{-1/4}. \tag{44}$$

In order to verify this result, we turn to Fig. 11 which shows the calculated h/H vs θ. Judging from the slopes of the curves, it is clear that the time interval separating the knee (θ_2) from the zero-solid limit (θ_3) decreases as the Rayleigh number increases. Indeed, by extrapolating the curves of Fig. 11 with straight lines downward it is possible to evaluate graphically the time interval $(\theta_3 - \theta_2)$ and to construct Fig. 12. We learn from the latter that $(\theta_3 - \theta_2)$ depends on Ra in the way anticipated by equation (44) (recall that in this first model l was assumed constant).

Alternatively, we may argue that at an intermediate stage in this last regime the liquid–solid interface advances such that both h and l decrease. It is simple to assume that h and l decrease at the same rate, in other words, that the interface advances while remaining parallel to itself (Fig. 10(b)). Equation (41) still applies, however, since $dh/dt \sim dl/dt$, equations (42)–(44) are now replaced in order by

$$Ra^{1/4} \sim -\left(\frac{h}{H}\right)^{1/4} \frac{d}{d\theta}\left(\frac{h}{H}\right) \tag{45}$$

$$\left(\frac{h}{H}\right)^{5/4} \sim 1 - Ra^{1/4}(\theta - \theta_2) \tag{46}$$

$$\theta_3 - \theta_2 \sim Ra^{-1/4}. \tag{47}$$

Equation (46) shows that h/H decreases almost linearly in θ, which is confirmed also by the shape of the curves presented in Fig. 11. Note further that the curvature of these curves is positive and that the same property is shared by the h/H function anticipated in equation (46). Most interesting, however, is that changing the solid shape model from Fig. 10(a) to Fig. 10(b) does not change the conclusion that the time of solid disappearance must scale as $Ra^{-1/4}$: like equation (44) earlier, equation (47) finds support in the data plotted in Fig. 12.

The Nusselt number scale consistent with equations (46) and (47) is $Nu \sim Ra_h^{1/4}$, which means

$$Nu \sim [1 - Ra^{1/4}(\theta - \theta_2)]^{3/5}. \tag{48}$$

This scaling law anticipates an increasingly steeper descent of the post-knee Nusselt number as Ra increases (Fig. 5). Furthermore, equation (48) describes a close-to-linear $Nu(\theta)$ function the curvature of which is negative: these features are both evident in Fig. 5, especially by viewing the post-knee curves drawn for $Ra = 10^6$ and 10^7.

Finally, we can think in terms of Fig. 10(c) and imagine a late enough stage when the solid has disappeared almost totally ($h \ll H$) leaving a nearly hori-

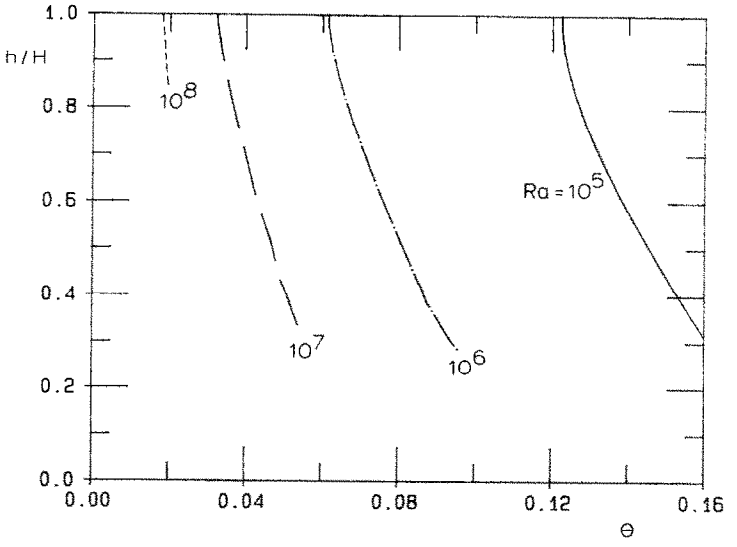

FIG. 11. Numerical results for the history of the height of the solid region, measured along the right-hand wall.

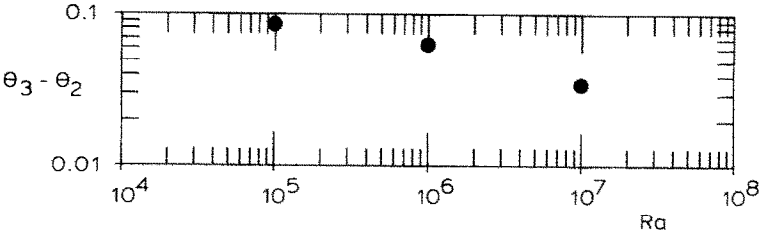

FIG. 12. The time interval needed by h/H to decrease from 1 to 0.

zontal 'lens', such that $h \ll l$. In this limit the heat transfer into the solid is impeded chiefly by the horizontal thermal boundary layer that forms over the lens of length l. The heat transfer part of this natural convection melting problem formed the subject of a classical paper by Clifton and Chapman [21]. It can be shown that in high Pr fluids the thermal boundary layer thickness scales as $lRa_l^{-1/5}$, where $Ra_l = Ra(l/H)^3$. The energy balance at the interface now reads

$$\frac{k(T_w - T_s)}{l} Ra_l^{1/5} \sim \rho h_{sf}\left(-\frac{dh}{dt}\right) \tag{49}$$

which eventually leads to

$$\left(\frac{H}{l}\right)^{2/5} Ra^{1/5} \sim -\frac{d}{d\theta}\left(\frac{h}{H}\right). \tag{50}$$

Assuming for the sake of comparison that the scenario of Fig. 10(c) prevails throughout the $\theta_2 < \theta < \theta_3$ regime, we learn from equation (50) that the time interval $(\theta_2 - \theta_3)$ would vary as $Ra^{-1/5}$. This conclusion does not differ much from the $Ra^{-1/4}$ dependence reached twice earlier, based on Figs. 10(a) and (b). An alternative argument would be to view the circulation near the shrinking solid as a corner flow of the type described in ref. [22]. Based on the results of this section, we believe that any convection model attached to a shrinking solid leads to conclusions that support the one outlined already, in other words, that the time scale of the solid vanishing phase is relatively insensitive to the assumed shape of the solid.

ADDITIONAL EFFECTS

The objective of this study has been to identify and sort out the most basic regimes and scales of the phenomenon of natural convection melting in a rectangular enclosure. It is an interesting and challenging problem because both the shape and the size of the liquid space change in time. Some of the scales mentioned in this paper had been identified previously in the literature; others had to be uncovered here for the first time in order to put together a coherent story of how these scales replace one another as the time increases. It is only because of this careful scaling work that we were able to construct, for example, the three-regime Nu correlation proposed in equations (36) and (37).

One limitation of a just completed study may very well become the objective of a future one. In this section we outline three possible extensions of the scaling theory formulated in this paper.

The effect of liquid thermal inertia (Stefan number)

In the present study we focused both theoretically and numerically on the limit of negligible thermal

inertia in the liquid space, that is, on the limit of small Stefan numbers. It is possible to rely on scaling one more time in order to reach towards the domain of large Stefan numbers. The heat transfer rate pumped through the left wall ($k\Delta T\,Nu$) is used both for advancing the position of the liquid–solid interface and for warming the newly created liquid up to the average temperature of the liquid space

$$k\Delta T\,Nu \sim \rho h_{sf} H \frac{ds_{av}}{dt} + \rho c \Delta T H \frac{ds_{av}}{dt}. \quad (51)$$

This translates into the scaling law

$$Nu \sim (1+Ste)\frac{dS_{av}}{d\theta} \quad (52)$$

or, more precisely

$$Nu = (1+C_1\,Ste)\frac{dS_{av}}{d\theta} \quad (53)$$

where C_1 is a numerical constant of order one. At finite Stefan numbers the melting rate $dS_{av}/d\theta$ trails the Nusselt number by the factor $(1+C_1\,Ste)$. In the pure convection regime, for example, we would have $Nu = c_1\,Ra^{1/4}$ and

$$\frac{dS_{av}}{d\theta} = \frac{c_1\,Ra^{1/4}}{1+C_1\,Ste}. \quad (54)$$

The C_1 constant could then be determined from a series of numerical simulations that do not neglect the effect of liquid thermal inertia.

The low Prandtl number limit

The scaling theory developed in this paper can be repeated for the case of natural convection melting of a solid the liquid phase of which has a Prandtl number considerably smaller than one. The feature that distinguishes this case from the '$Pr > 1$' case assumed in this paper is the thickness of the thermal boundary layer in the convection zone of height z. In place of equation (18) we write (cf. p. 120 of ref. [5], the case '$Pr < 1$')

$$\delta_z \sim z\,Pr^{-1/4}\,Ra_z^{-1/4} \quad (55)$$

which leads to a new scaling law for the convection zone height

$$z \sim H\,Ra\,Pr\,\theta^2. \quad (56)$$

Comparing this result with equation (19) we note that the shift from the high Prandtl number limit to the low Prandtl number limit is accompanied by the replacement of Ra with the group $Ra\,Pr$ in the analysis. Indeed, if we repeat the analytical steps contained between equations (20)–(30) we obtain the following results for the Nusselt number scaling law in the mixed heat transfer regime:

$$Nu \sim \theta^{-1/2} + Ra\,Pr\,\theta^{3/2} \quad (57)$$

the time marking the end of the mixed regime

$$\theta_1 \sim (Ra\,Pr)^{-1/2} \quad (58)$$

the coordinates of the minimum in the $Nu(\theta)$ curve

$$Nu_{min} \sim (Ra\,Pr)^{1/4} \quad (59)$$

$$\theta_{min} \sim (Ra\,Pr)^{-1/2} \quad (60)$$

the scaling laws for the convection dominated regime

$$Nu \sim (Ra\,Pr)^{1/4} \quad (61)$$

$$s_{av} \sim H(Ra\,Pr)^{1/4}\theta \quad (62)$$

and, finally, the time marking the end of the convection dominated regime

$$\theta_2 \sim \frac{L}{H}(Ra\,Pr)^{-1/4}. \quad (63)$$

The smooth correlations recommended for the first three regimes (Figs. 1(a)–(c)) have the form

$$Nu = (2\theta)^{-1/2} + [c_1'(Ra\,Pr)^{1/4} - (2\theta)^{-1/2}] \times [1 + (c_2'\,Ra^{3/4}\,Pr^{3/4}\,\theta^{3/2})^n]^{1/n} \quad (64)$$

$$S_{av} = \{[(2\theta)^{1/2}]^m + [c_1'(Ra\,Pr)^{1/4}\theta]^m\}^{1/m} \quad (65)$$

in which the exponents (n, m) and the constants of order one (c_1', c_2') remain to be determined from comparisons with future laboratory measurements and numerical simulations of $Pr < 1$ convection in cavities carved by melting.

The effect of transient conduction in the solid phase

The case where the solid is at a temperature lower than the melting temperature is important because in laboratory experiments and in actual applications it is difficult to maintain the solid uniformly at the melting temperature. We mention this case because it marks the end of the territory we can cover with the scaling theory constructed in this paper. In the preceding subsections we were able to extend the theory by varying the liquid Stefan number and Prandtl number because, despite these extensions, the nature of the heat transfer mechanisms remained as theorized in Fig. 1. If one is to consider the additional effect of conduction in the solid, one must construct a new scenario in place of Fig. 1. It is not a question of merely introducing a new dimensionless group (the solid Stefan number), rather, it is the challenge of recognizing the time scales of the heat transfer regimes that keep changing on both sides of the liquid–solid interface. In this effort, easy access to numerical experiments that account for conduction in the solid (i.e. unlike the present ones) is essential.

Acknowledgements—This study was conducted during Peter Jany's visit as a NATO Postdoctoral Fellow at Duke University. The financial support received from NATO through the 'Deutscher Akademischer Austausch Dienst' (DAAD) is gratefully acknowledged. Adrian Bejan's research was

supported by the Electric Power Research Institute Contract No. RP 8006-4 under the management of Dr Jong H. Kim.

REFERENCES

1. R. Viskanta, Phase-change heat transfer. In *Solar Heat Storage: Latent Heat Materials* (Edited by G. A. Lane), pp. 153–222. CRC Press, Boca Raton, Florida (1983).
2. R. Viskanta, Natural convection melting and solidification. In *Natural Convection: Fundamentals and Applications* (Edited by S. Kakac, W. Aung and R. Viskanta), pp. 845–877. Hemisphere, Washington, DC (1985).
3. B. W. Webb and R. Viskanta, On the characteristic length scale for correlating melting heat transfer data, *Int. Commun. Heat Mass Transfer* **12,** 637–646 (1985).
4. U. Grigull and H. Sandner, *Heat Conduction* (Translated by J. Kestin), pp. 144–150. Springer, Berlin (1984).
5. A. Bejan, *Convection Heat Transfer*. Wiley, New York (1984).
6. G. K. Batchelor, Heat transfer by free convection across a closed cavity between vertical boundaries at different temperature, *Q. Appl. Math.* **12,** 209–233 (1954).
7. D. E. Cormack, L. G. Leal and J. Imberger, Natural convection in a shallow cavity with differentially heated end walls. Part 1: asymptotic theory, *J. Fluid Mech.* **65,** 209–229 (1974).
8. J. H. Lienhard, On the commonality of equations for natural convection from immersed bodies, *Int. J. Heat Mass Transfer* **16,** 2121–2123 (1973).
9. A. Bejan, Buckling flows: a new frontier in fluid mechanics. In *Annual Review of Numerical Fluid Mechanics and Heat Transfer* (Edited by T. C. Chawla), Vol. 1, Chap. 5, pp. 262–304. Hemisphere, Washington, DC (1987).
10. C.-J. Ho and R. Viskanta, Heat transfer during melting from an isothermal vertical wall, *J. Heat Transfer* **106,** 12–19 (1984).
11. P. Jany and A. Bejan, Scaling theory of melting with natural convection in an enclosure, Report DU-AB-6, Dept. Mech. Engng and Materials Sci., Duke University (1987).
12. N. W. Hale, Jr. and R. Viskanta, Photographic observation of the solid–liquid interface motion during melting of a solid heated from an isothermal vertical wall, *Lett. Heat Mass Transfer* **5,** 329–337 (1978).
13. A. Kassinos and J. Prusa, Effects of density change and subcooling on the melting of a solid in a rectangular enclosure, *Proc. 8th Int. Heat Transfer Conf.*, San Francisco (1986).
14. A. Gadgil and D. Gobin, Analysis of two-dimensional melting in rectangular enclosures in presence of convection, *J. Heat Transfer* **106,** 20–26 (1984).
15. M. Bareiss and H. Beer, Experimental investigation of melting heat transfer with regard to different geometric arrangements, *Int. Commun. Heat Mass Transfer* **11,** 322–333 (1984).
16. M. Okada, Melting from a vertical plate between insulated top and bottom surfaces, *Proc. ASME/JSME Thermal Engng Joint Conf.*, Vol. 1, pp. 281–288. American Society of Mechanical Engineers (1983).
17. M. Okada, Analysis of heat transfer during melting from a vertical wall, *Int. J. Heat Mass Transfer* **27,** 2057–2066 (1984).
18. C. Bénard, D. Gobin and F. Martinez, Melting in rectangular enclosures: experiments and numerical simulations, *J. Heat Transfer* **107,** 794–803 (1985).
19. S. W. Churchill, The development of theoretically based correlations for heat and mass transfer, *Lat. Am. J. Heat Mass Transfer* **7,** 207–229 (1983).
20. A. Bejan, Note on Gill's solution for free convection in a vertical enclosure, *J. Fluid Mech.* **90,** 561–568 (1979).
21. J. V. Clifton and A. J. Chapman, Natural-convection on a finite-size horizontal plate, *Int. J. Heat Mass Transfer* **12,** 1573–1584 (1969).
22. S. Kimura and A. Bejan, Natural convection in a differentially heated corner region, *Physics Fluids* **28,** 2980–2989 (1985).

THEORIE D'ECHELLES DE LA FUSION AVEC CONVECTION NATURELLE DANS UNE ENCEINTE

Résumé—Cette étude identifie les échelles et les régimes les plus fondamentaux du phénomène de fusion avec convection naturelle dans une enceinte chauffée latéralement. Dans une première partie, la méthode des échelles est utilisée pour montrer que le phénomène concerne quatre régimes: (a) la conduction pure, (b) le régime mixte dans lequel la zone supérieure du liquide est régit par la convection et la zone inférieure par la conduction, (c) le régime de convection et enfin, (d) le régime de "solide compact". Pour les trois premiers régimes, la théorie prédit une courbe de nombre de Nusselt en fonction du temps qui a une allure semblable à l'isotherme de van der Waals, en particulier, un Nu minimum de l'ordre de $Ra^{1/4}$ à l'instant $Ste\,Fo$ de l'ordre de $Ra^{-1/2}$ où Ste est le nombre de Stefan du liquide surchauffé et Fo le nombre de Fourier basé sur H. La position correspondante du front moyen a un point d'inflexion au temps proche de $Ra^{-1/2}$. La théorie montre aussi que pendant le quatrième régime le solide disparait pendant un intervalle de temps de l'ordre de $Ra^{-1/4}$. La seconde partie de l'étude concerne les expériences numériques dont le but est de vérifier que la théorie construite dans la première partie est correcte. Les simulations numériques sont basées sur l'approximation du front et de convection naturelle quasi-stationnaires. Le domaine parametrique couvert par ces simulations est $0 \leqslant Ra \leqslant 10^8$, $0 < Ste\,Fo < 0{,}2$, $Pr = 50$ et $H/L = 1$, où L est la dimension horizontale de la cavité et Ra le nombre de Rayleigh basé sur H. Des formules pour Nu et la position du front de fusion en fonction du temps sont données en combinant les conclusions théoriques et numériques de l'étude.

THEORIE ZUR BEURTEILUNG DES SCHMELZVORGANGS MIT NATÜRLICHER KONVEKTION IN EINER EINSCHLIESSUNG

Zusammenfassung—In dieser Arbeit werden die grundsätzlichen Bereiche beim Schmelzen unter natürlicher Konvektion in einem seitlich beheizten Hohlraum dargestellt. Im ersten Teil der Untersuchung wird mittels einer Größenordnungs-Abschätzung gezeigt, daß das Phänomen aus einer Abfolge von vier Bereichen besteht: (a) Gebiet der reinen Wärmeleitung, (b) Mischgebiet, in dem im oberen Teil der Flüssigkeit Konvektion und im unteren Teil Wärmeleitung vorherrscht, (c) Konvektionsgebiet und schließlich (d), das letzte, sogenannte "shrinking solid"-Gebiet. Für die ersten drei Bereiche liefert die Skalierungs-Theorie eine zeitabhängige Nusselt-Zahl, die ähnliche Eigenschaften wie die van der Waals-Isothermen aufweist und insbesondere ein eindeutiges Minimum der *Nu*-Zahl im Bereich $Ra^{1/4}$ bei der Zeit *Ste Fo* im Bereich von $Ra^{-1/2}$ zeigt. Dabei ist *Ste* die Stefan-Zahl der überhitzten Flüssigkeit und *Fo* die mit *H* gebildete Fourier-Zahl. Die korrespondierende mittlere Lage der Schmelzfront hat einen Wendepunkt zu einer Zeit bei $Ra^{-1/2}$. Die Theorie zeigt weiter, daß im vierten Bereich die festen Bestandteile in einem *Ste Fo* Zeitintervall von $Ra^{-1/4}$ verschwinden. Den zweiten Teil der Arbeit bilden numerische Experimente, die die im ersten Teil aufgestellte Theorie verifizieren sollen. Die numerischen Simulationen beruhen auf der Näherungsmethode der quasistationären Front und der Annahme quasistationärer natürlicher Konvektion. Die hier durchgeführten Parameterstudien decken einen Bereich $0 \leqslant Ra \leqslant 10^8$, $0 < Ste\ Fo < 0{,}2$; $Pr = 50$ und $H/L = 1$ ab, wobei *L* die horizontale Abmessung des Hohlraums und a die auf *H* bezogene Rayleigh-Zahl ist. Es werden geschlossene Korrelationen für die Nusselt-Zahl und die Orts-Zeit-Funktion der Schmelzfront durch Kombination der theoretischen und numerischen Ergebnisse aufgestellt.

ТЕОРИЯ ПОДОБИЯ ПРОЦЕССОВ ПЛАВЛЕНИЯ ПРИ ЕСТЕСТВЕННОЙ КОНВЕКЦИИ В ЗАМКНУТОЙ ПОЛОСТИ

Аннотация—Определены наиболее характерные величины и режимы плавления с учетом естественной конвекции в замкнутой полости, нагреваемой сбоку. В первой части исследования используется метод теории подобия чтобы показать, что явление плавления включает четыре последовательно проходящих режима: (а) теплопроводность, (б) смешанный режим, в котором для верхней части жидкости справедливы законы конвективного теплообмена, а нижней—законы теплопроводности, (в) кондуктивный теплообмен и, наконец, (г) последний режим или "усадка твердого тела". Для первых трех режимов с помощью теории подобия предсказана зависимость числа Нуссельта от времени, которая подобна изотерме Ван дер Ваальса, в частности, минимум Нуссельта порядка $Ra^{1/4}$ соответствует времени *Ste Fo* порядка $Ra^{-1/2}$, где *Ste*—число Стефана для перегретой жидкости и *Fo*—число Фурье, основанное на *H*. Соответствующее среднее положение фронта плавления имеет точку перегиба при времени порядка $Ra^{-1/2}$. Теория показывает далее, что в четвертом режиме твердое тело исчезает за время порядка $Ra^{-1/4}$. Во второй части работы представлены численные расчеты, цель которых проверить правильность теории, созданной в первой части. Численное моделирование основано на приближении квазистационарного фронта и предположении о квазистационарной естественной конвекции. Моделирование выполнено в следующих областях параметров: $0 \leq Ra \leq 10^8$, $0 < Ste\ Fo < 0{,}2$, $Pr = 50$ и $H/L = 1$, где *L*—горизонтальный размер полости, а *Ra*—число Рэлея, основанное на *H*. В результате объединения теоретических и численных результатов получены соотношения, близкие по форме, для зависимостей числа Нуссельта и положения фронта плавления от времени.